

Journal of Biomedical Optics

SPIEDigitalLibrary.org/jbo

Nondestructive inspection of phase transformation in zirconia-containing hip joints by confocal Raman spectroscopy

Wenliang Zhu
Nobuhiko Sugano
Giuseppe Pezzotti



SPIE

Nondestructive inspection of phase transformation in zirconia-containing hip joints by confocal Raman spectroscopy

Wenliang Zhu,^{a,b} Nobuhiko Sugano,^b and Giuseppe Pezzotti^a

^aKyoto Institute of Technology, Ceramic Physics Laboratory and Research Institute for Nanoscience, Sakyo-ku, Matsugasaki, 606-8585 Kyoto, Japan

^bOsaka University Medical School, Department of Orthopedic Surgery, 2-2 Yamadaoka, 565-0871 Suita, Japan

Abstract. Environmental metastability of zirconia (ZrO₂) ceramic in the human body [represented by a tetragonal-to-monoclinic ($t \rightarrow m$) phase transformation] takes place on the surface of the artificial joint and proceeds with time toward its interior. Its quantitative characterization is mandatory for the safety of joint implants and consists of the assessment of the in-depth monoclinic profile fraction as compared to that of the initially untransformed material. We attempt to fully establish a characterization protocol and present two different nondestructive approaches for resolving highly graded phase-transformation profiles along the hip-joint subsurface by confocal Raman microprobe technique. A series of partially transformed tetragonal zirconia polycrystal and zirconia-toughened alumina ceramics are used as screening samples. Probe biases could be eliminated and the real transformation profiles retrieved through a deconvolution procedure of Raman experimental data collected as a function of pinhole aperture and focal depth, respectively. Confirmation of the confocal assessments was made by a destructive cross-sectional inspection by both laser optical microscope and Raman spectral line scans. This study unveils for the first time the real quantitative amount of surface phase-transformation fractions and the related subsurface profiles in zirconia-based retrieved medical samples. © 2013 Society of Photo-Optical Instrumentation Engineers (SPIE) [DOI: 10.1117/1.JBO.18.12.127002]

Keywords: Raman spectroscopy; phase transformation; artificial hip joints; nondestructive analysis.

Paper 130676R received Sep. 17, 2013; revised manuscript received Oct. 27, 2013; accepted for publication Oct. 29, 2013; published online Dec. 2, 2013.

1 Introduction

Since the middle of the 1980s, zirconia-based ceramics, such as yttria-stabilized tetragonal zirconia polycrystal (Y-TZP), alumina-reinforced zirconia ceramics, and the latest-generation, zirconia-toughened alumina composites (ZTA), have been widely used as load-bearing components in artificial joints due to their excellent mechanical properties.¹⁻³ Stabilized TZP are subjected to aging, that is, polymorphic transformation from the tetragonal to the monoclinic phase, upon exposure to biological environment (e.g., in a low-temperature humid atmosphere). As a result, in addition to the problem of possible tissue inflammation, which is also one type of failure in these implants, problems of wear and *in vivo* surface deterioration might also occur, and this degradation phenomenon represents one main detrimental aspect of material metastability.⁴ If uncontrolled, it might potentially increase the roughness of the joint surface with detrimental consequences on the overall joint lifetime.⁵ In particular, phase transformation, which progressively develops from the joint surface toward the in-depth direction, induces pathological complications in the joint and has been indicated as one cause of its failure.^{6,7}

For the spectroscopic analysis of phase transformation in the zirconia-based ceramic hip joints, Raman microprobe spectroscopy has been recognized as a powerful tool, which is capable of providing a significant piece of information on phase composition, volume fraction, and residual stress in the components.⁸⁻¹⁸

However, the information searched for in a Raman spectrum is usually convoluted within spectroscopic outputs, such as the relative intensity, the shift, or width changes of the observed spectral bands. As a result, inconsistency in the experimentally measured data, especially the measured apparent phase volume fraction and residual stress magnitude, is often seen when the instrumental conditions are altered (e.g., change in the objective lens, laser spot size, slit aperture, or even number of monochromator, etc.). Accordingly, the scattering of the obtained data sets of phase-transformation profiles without clarification of the probe geometry may result in a misunderstanding of the actual state of the biomaterial surface and an incorrect lifetime prediction for surface stability.

Since the spectroscopic information is averaged within the probe volume along both the in-plane and the in-depth directions, the spectral results depend on the transparency of the probed material and on the probe depth. In ZrO₂ ceramics, the laser penetration depth may be as deep as several hundreds of microns, and significant averaging is usually observed in the collected Raman spectra.¹⁹ Therefore, to quantitatively reveal the physical, chemical, or mechanical information contained in a Raman spectrum, additional deconvolution procedures need to be established. In this paper, we studied two different approaches with a mathematical deconvolution method for obtaining highly graded phase-transformation profiles along the hip-joint subsurface in various TZP and ZTA samples by confocal Raman microprobe technique: the laser defocusing method (LDM) and the controlled pinhole aperture method (CPAM). Preliminary to this data treatment procedure, we

Address all correspondence to: Giuseppe Pezzotti, Kyoto Institute of Technology, Ceramic Physics Laboratory and Research Institute for Nanoscience, Sakyo-ku, Matsugasaki, 606-8585 Kyoto, Japan. Tel: +81-75-724 7568; Fax: +81-75-724 7568; E-mail: pezzotti@kit.ac.jp

show a characterization of the probe response function for selected Raman bands of both tetragonal and monoclinic ZrO_2 polymorphs in TZP and ZTA, according to the variation of Raman spectral intensity as a function of focal depth. Based on the laser probe-sample interaction, theoretical analysis for interpreting experimental data due to probe convolution was performed on a series of TZP samples subjected to different exposure times in autoclave, and the real property distributions were retrieved through a best-fitting iterative routine of Raman experimental data collected on the same material as a function of pinhole aperture and focal depth, respectively. Reliability of the obtained results was further examined and confirmed by a destructive cross-sectional inspection by both laser optical microscope and Raman spectral line scans. Finally, applications of the proposed methods on two kinds of commercially available ZTA hip joints and a retrieved one were carried out, showing a strong dependence of the phase stability of the material in hydrothermal environment on the contents of stabilizing agents added to the raw powder mixtures.

2 Theoretical Background

When a zirconia-based material is irradiated with a focused laser, Raman and/or fluorescence lines will be generated at any local radiated region. Accordingly, upon focusing the laser at a location (x_0, y_0, z_0) , the observed spectrum is obtained by combining all the spectra originating from different points within the analyzed region, and the contribution to the observed spectrum of the light scattered from the point (x, y, z) is expressed by the probe response function (PRF).²⁰⁻²²

$$\begin{aligned} G(x, y, z) &= G(x, y, x_0, y_0) \times G(z, z_0) \\ &\propto \frac{1}{B} \exp\left[-2 \frac{(x-x_0)^2 + (y-y_0)^2}{B^2}\right] \\ &\times \frac{p^2}{(z-z_0)^2 + p^2} \exp(-2\alpha_{\text{eff}}z), \end{aligned} \quad (1)$$

where p is the probe response parameter and α_{eff} is the effective absorption coefficient of the incident light for the investigated specimen, which incorporates the effect of inhomogeneous light scattering in polycrystals. B is the radius of the waist of the laser beam, which is approximately given by $B(z) = [(z/\{\cot[\sin^{-1}(\text{NA}/n)]\})^2 + B_0^2]^{1/2}$, with n being the refractive index of the material, NA is the numerical aperture of the objective lens, and B_0 is the in-plane focal spot radius.²³ The Cartesian coordinates are taken with their origin on the sample free surface: the z axis is perpendicular to the free surface and oriented toward the sample subsurface, while the x and y axes are arbitrarily located on the free surface. Consequently, the final collected line shape can be expressed as

$$\begin{aligned} I_{\text{obs}}(x_0, y_0, z_0) &\propto \int_{x=-\infty}^{+\infty} \int_{y=-\infty}^{+\infty} \int_{z=0}^{z=t_h} I(\omega) \times G(x, y, x_0, y_0) \\ &\times G(z, z_0) dx dy dz, \end{aligned} \quad (2)$$

where t_h is the thickness of the sample and $I(\omega) \propto [A^2/(\omega - \omega_p)^2 + A^2]$ represents the local spectral line shape, with ω_p being the band position and A the half-width.

In the case of the presence of spatial distribution of any measurable spectroscopic property, $\wp(x, y, z)$ (e.g., band intensity, band width, or band position altered by the distribution of stress,

temperature, defect, etc.), with each location possessing a specific local property, an overall apparent property is observed by the averaging effect of the Raman probe. When the Raman probe is centered at the location $P_0(x_0, y_0, z_0)$, the observed property value, $\bar{\wp}(x_0, y_0, z_0)$, is indeed a weighted average of the real property, $\wp(x, y, z)$, within the probe volume, as follows:

$$\begin{aligned} \bar{\wp}(x_0, y_0, z_0) &= \frac{\int_{x=-\infty}^{+\infty} \int_{y=-\infty}^{+\infty} \int_{z=0}^{t_h} \wp(x, y, z) G(x, y, z, x_0, y_0, z_0) dx dy dz}{\int_{x=-\infty}^{+\infty} \int_{y=-\infty}^{+\infty} \int_{z=0}^{t_h} G(x, y, z, x_0, y_0, z_0) dx dy dz}. \end{aligned} \quad (3)$$

Given the relatively high transparency of ZrO_2 ceramics, a laser microprobe is able to bring us information from in-depth portions of the material. By neglecting the property distribution within any of the xy planes parallel to the free surface of the sample, the PRF can be simplified (referred to as the in-depth PRF) as follows:

$$G(z, z_0) \propto \exp(-2\alpha_{\text{eff}}z) \frac{p^2}{(z-z_0)^2 + p^2}. \quad (4)$$

The observed spectral intensity at band maximum can then be obtained according to a simple integration procedure of the PRF, as follows:

$$I_{\text{obs}}(\omega_p) \propto \int_0^{\infty} \exp(-2\alpha_{\text{eff}}z) \frac{p^2}{(z-z_0)^2 + p^2} dz, \quad (5)$$

where $I_{\text{obs}}(\omega_p)$ is the intensity at maximum of the observed Raman line. From the variation of the observed intensity with a change in the focal position, z_0 , the probe-related parameters, p and α_{eff} , can be determined according to Eq. (5). Once the PRF characterizing the interaction between the Raman probe and the studied material is known, Eq. (3) can be quantitatively used for spatial deconvolution of spectroscopic data [namely, to derive the real property distribution, $\wp(x, y, z)$, from the (averaged) measured one].

In assessing the surface of ceramic joints, a probe of large dimensions along the depth will fail in detecting the presence of steep subsurface gradients, and a shallow probe configuration is highly desirable. The in-depth resolution of the Raman probe can be improved by placing a confocal pinhole at the back-focal image plane to partly cut off the light scattered from outside the laser focal area.^{24,25} Accordingly, only signals from regions close to the focal plane are brought to the detector. By employing this technique, discrete z -planes can be probed with relatively high in-depth spatial resolution, but Eq. (5) will experience a more complicated morphology because of the incorporation of the collection solid angle, Ω , in response to the change in the geometry of the optical probe. The collection solid angle depends on the pinhole diameter, Φ , the numerical aperture (NA), the diameter, D , the focal length, f , of the objective lens, the refractive index of the material, n , as well as the focal in-depth position, z_0 . The complete mathematical derivation and description of PRF in the presence of a confocal probe have been given elsewhere,^{21,24,25} and here we briefly report the salient parts of this derivation.

When the focal plane is placed on the sample surface ($z_0 = 0$), approximately by neglecting the off-axis effect,

Eq. (2) can be rearranged to give the observed intensity, I_{obs} , as follows:

$$I_{\text{obs}}(\omega_p) \propto \int_0^t \int_0^{\rho_{\text{max}}} \frac{1}{B(z)} \exp\left[-2\frac{r^2}{B(z)}\right] r dr \times \Omega(\rho_{\text{max}} \leq \rho_0) \times \exp(-2\alpha_{\text{eff}}z) \frac{p^2}{z^2 + p^2} dz + \int_t^\infty \int_0^{\rho_0} \frac{1}{B(z)} \exp\left[-2\frac{r^2}{B(z)}\right] r dr \times \Omega(\rho_{\text{max}} \geq \rho_0) \exp(-2\alpha_{\text{eff}}z) \frac{p^2}{z^2 + p^2} dz. \quad (6)$$

Considering the competitive effects of the lens NA and of the pinhole aperture, the collection solid angle Ω can be expressed as follows:

$$\Omega = 2\pi \left[1 - \frac{z}{\sqrt{z^2 + \rho_0^2}} \right] \quad (\rho_{\text{max}} \geq \rho_0) \quad (7)$$

$$\Omega = 2\pi \left(1 - \frac{z}{\sqrt{z^2 + \rho_{\text{max}}^2}} \right) \quad (\rho_{\text{max}} \leq \rho_0), \quad (8)$$

where ρ_{max} is the maximum transverse ray aberration from the optical axis (determined by NA); $2\rho_0$ is the virtual back-image of the confocal pinhole (with a diameter) in the sample focal plane, given by the relation $2\rho_0 = \Phi/(\text{MP} \times \text{GF})$, where MP is the magnification power of the objective and GF is the enlargement factor (1.4); t is a threshold z value at which the effects of the lens NA and pinhole aperture are equivalent (i.e., $\rho_0 = \rho_{\text{max}}$, and $\Omega\rho_0 = \rho_{\text{max}}$), which can be determined directly from the optical geometry for the case of $z_0 = 0$.²²

$$t = \rho_0 \sqrt{(n^2 - 1) + \left(\frac{f}{D/2 - \rho_0}\right)^2 n^2}. \quad (9)$$

Accordingly, provided the above geometrical limitation is respected, by changing the pinhole diameter, Φ , (i.e., ρ_0), the real property distribution, $\wp(z)$, can, to a degree of precision, be derived from the deconvolution of the (averaged) measured one as follows:

$$\bar{\wp}(\Phi) = \frac{\int_0^t \wp(z) \times \Omega(\rho_{\text{max}} \leq \rho_0) G(z) dz + \int_t^\infty \wp(z) \times \Omega(\rho_{\text{max}} \geq \rho_0) G(z) dz}{\int_0^t \Omega(\rho_{\text{max}} \leq \rho_0) G(z) dz + \int_t^\infty \Omega(\rho_{\text{max}} \geq \rho_0) G(z) dz}. \quad (10)$$

It should be noted that this method is constrained by the finite depth of the probe when the focal plane is placed on the sample surface; i.e., it is only applicable to the cases where the transformation depth is much smaller than the maximum probe depth, z_d , which corresponds to a maximum value of Φ or ρ_0 and can be calculated by solving the following equation:

$$\frac{\int_0^{z_d} \Omega(\rho_{\text{max}} \leq \rho_0) G(z) dz}{\int_0^\infty \Omega(\rho_{\text{max}} \leq \rho_0) G(z) dz} \approx \frac{\int_0^{z_d} G(z) dz}{\int_0^\infty G(z) dz} = 0.9, \quad (11)$$

where we shall consider the 90% of the maximum band intensity as a threshold value for the intensity distribution.

Fortunately, such constraint can be removed by using a complementary method, the so-called defocusing method, i.e., a gradual translation of the focal plane from the surface toward the internal part of the material to probe sharp phase-transformation gradients along the material subsurface. When the incident laser is focused inside the material ($z_0 > 0$), for a small pinhole aperture, at locations where $z < z_0$, the collection solid angle is determined by the objective lens [i.e., Eq. (8)], while at locations where $z > z_0$, Ω is mainly determined by the virtual back-image $2\rho_0$ of the confocal pinhole in the sample focal plane and can be approximated by the following function:

$$\Omega(z > z_0) = 2\pi \left[1 - \frac{1}{\sqrt{1 + \rho_0^2/(z - z_0)^2}} \right]. \quad (12)$$

Accordingly, the observed intensity, $I_{\text{obs}}(z_0)$, can be deduced as follows:

$$I_{\text{obs}}(z_0) \propto \int_0^{z_0} \Omega(z \leq z_0) \frac{p^2}{(z - z_0)^2 + p^2} \exp(-2\alpha_{\text{eff}}z) dz + \int_{z_0}^\infty \Omega(z > z_0) \frac{p^2}{(z - z_0)^2 + p^2} \exp(-2\alpha_{\text{eff}}z) dz, \quad (13)$$

and with the change of the focal plane z_0 , the convolution of the real property distribution in the probe volume can be given by

$$\bar{\wp}(z_0) = \frac{\int_0^{z_0} \wp(z) \times \Omega(z \leq z_0) G(z) dz + \int_{z_0}^\infty \wp(z) \times \Omega(z > z_0) G(z) dz}{\int_0^{z_0} \Omega(z \leq z_0) G(z) dz + \int_{z_0}^\infty \Omega(z > z_0) G(z) dz}. \quad (14)$$

Therefore, Eqs. (10) and (14) can be used to determine the real property through a best-fitting iterative routine of Raman experimental data collected on the same material as a function of ρ_0 and z_0 , respectively, for a confocal Raman probe.

3 Experimental Procedure

A series of polycrystalline tetragonal ZrO_2 containing a small amount (3 mol%) of Y_2O_3 as a stabilizing agent and two different kinds of commercially available ZTA ceramics consisting of 80 vol% Al_2O_3 (denoted by ZTA-A and ZTA-D) were used in this study. The 3Y-TZP joints belonged to an early generation manufacturing product with the material grain size being $\sim 1.0 \mu\text{m}$, while the modern ZTA composite joints have a grain size $< 1.0 \mu\text{m}$. A very small fraction of stabilizing agents Y_2O_3 and Cr_2O_3 exist in the raw materials of ZTA-D, but none in ZTA-A. The samples were exposed in a saturated vapor

atmosphere of an autoclave at different temperatures and for different times to make surface phase transformation progressing. An *in vivo* ZTA ball (implanted for hip joint) retrieved as a load-bearing component against a polyethylene cup was also investigated by Raman spectroscopy.

Raman spectra were collected at room temperature by a triple-monochromator (T-64000, Jovin-Ivon/Horiba Group, Kyoto, Japan) equipped with a charge-coupled device detector and analyzed by commercially available software (Labspec, Horiba/Jobin-Yvon, Kyoto, Japan). A confocal pinhole with an aperture-diameter of 100 μm was placed in the optical circuit to exclude photons scattered from out-of-focus regions of the probe. The schematic draft of the optical probe in confocal configuration is available in our previous papers.^{12,22} An automated sample stage was employed, making it possible to record spectra at each depth with focusing above or below the sample surface or to map spectra with lateral line scanning on surfaces or on cross-sections of the samples that underwent $t \rightarrow m$ phase transformation. No significant difference could be observed in the Raman spectral profiles collected at about 10 different locations selected on the surface of the autoclaved samples. This can be attributed to the larger size (i.e., in volume) of the adopted Raman probe as compared to the respective grain sizes of the investigated materials. Phase-transformation profiles collected by translating the focal plane along the in-depth direction were spatially deconvoluted according to a mathematical algorithm solved by commercially available software (MATHEMATICA 5.0, Wolfram Research Inc., Champaign, Illinois).

4 Results and Discussion

4.1 Raman Spectra and PRFs in 3Y-TZP and ZTA Ceramics

Figure 1(a) shows typical Raman spectra, as collected separately in an as-received 3Y-TZP, a fully transformed 3Y-TZP, and a partly transformed 3Y-TZP (PT-TZP), which mainly consist of $t\text{-ZrO}_2$, $m\text{-ZrO}_2$, and both $m\text{-}$ and $t\text{-ZrO}_2$, respectively. Typical Raman spectra collected in as-received, fully transformed, and PT ZTA composites are shown in Fig. 1(b). For comparison, typical Raman spectrum of polycrystalline alumina is also shown in Fig. 1(b). The details about the assignments of the observed Raman bands have been published in previous papers for $t\text{-ZrO}_2$,

$m\text{-ZrO}_2$, and alumina.^{26,27} As can be seen, taking advantage of the intense singlet located at 150 cm^{-1} and the relatively sharp doublet located at about 180 to 190 cm^{-1} (peculiar of the tetragonal and the monoclinic phases, respectively), examination of phase transformation of zirconia is made possible for PT-TZP. Similar phenomena can be observed in the ZTA composites. For the PT-ZTA composite, besides the presence of the $m\text{-ZrO}_2$ and $t\text{-ZrO}_2$ bands, a peculiar peak of alumina located at 417 cm^{-1} is also observable. Note that the monoclinic bands are clearly separated from those of the tetragonal polymorph and can be used as sensors for probe/phase/stress evaluation.

In practice, the amount of $t \rightarrow m$ phase transformation can be estimated from the relative intensity of selected tetragonal and monoclinic bands. The volume fraction of monoclinic phase, V_m , can be calculated according to the following equation:²⁸

$$V_m = \frac{0.5(I_m^{180} + I_m^{190})}{0.5(I_m^{180} + I_m^{190}) + 2.2I_t^{150}}, \quad (15)$$

where I represents the intensity of Raman bands (whose subscripts m and t denote the monoclinic and the tetragonal polymorphs, respectively, and superscripts are representative of the band spectral position). Since the value of the apparent property, V_m , is strongly dependent on probe size (i.e., because of the averaging effect of the Raman probe), Eq. (3) should be applied for probe deconvolution to retrieve the real property, which however needs a prior understanding of the PRFs of the investigated bands for the zirconia-based ceramics.

In fact, a laser microprobe focused on the joint surface may reach depths along the subsurface that may be much greater than the laser spot diameter. The depth PRF can be determined from the variation of the spectral band intensity with the focal position in the laser-defocusing measurements, while the lateral PRF can be determined by moving the probe across a sharp edge of the sample and recording the intensity as a function of the distance from the edge. Figure 2(a) shows the experimental data of the laser-defocusing measurements, retrieved separately in untreated or fully transformed 3Y-TZP and ZTA samples for PRF, $G(z, z_0)$, of the Raman bands located at 150 and 180 cm^{-1} (representative of the tetragonal and of the monoclinic polymorphs, respectively). Data sets obtained at other different locations showed a negligible difference in the defocusing profile because of a large probe size with respect to the respective

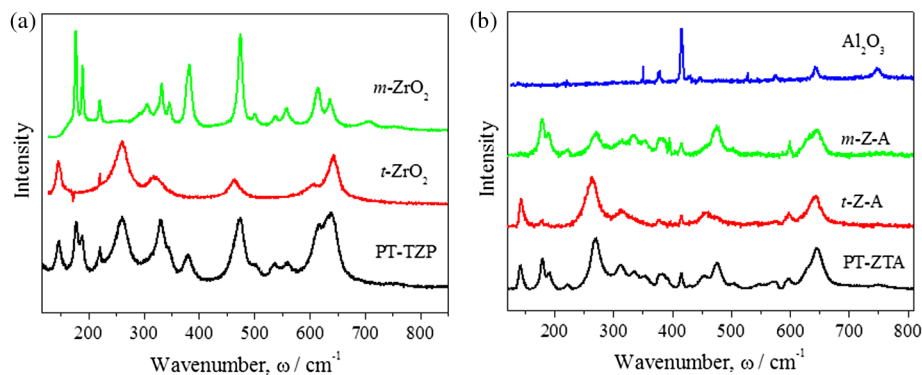


Fig. 1 Raman spectra collected respectively on as received, fully transformed, and partly transformed (a) 3Y-tetragonal zirconia polycrystal (TZP) and (b) zirconia-toughened alumina (ZTA) ceramics.

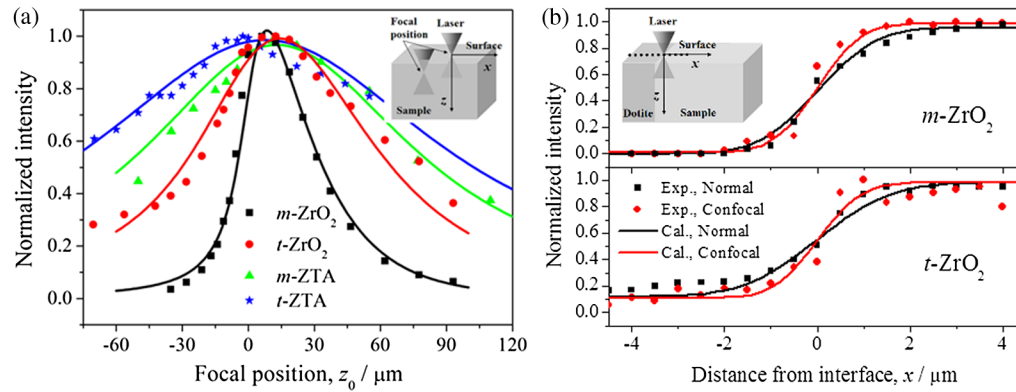


Fig. 2 Variation of normalized intensities of the 146 and the 178 cm^{-1} Raman bands as a function of (a) defocusing depth with respect to the sample surface, z_0 obtained in untreated or fully transformed 3Y-TZP and ZTA ceramics and (b) the distance from the interface between ZTA and dotite in the line scans on as received or fully transformed 3Y-TZP samples. The insets of (a) and (b) show schematic drafts of the in-depth defocus measurement and the in-plane line scans, respectively. The error involved in the Raman measurements is comparable with the size of the symbols used in the plots.

grain size. An explanatory draft of the interaction between the Raman microprobe and the near-surface portion of a hip joint is shown in inset to this figure. The band intensity was normalized with respect to the observed maximum intensity. A positive z_0 value refers to a translation of the focal plane below the free surface. Note that the focal position inside the sample is altered by the refractive index n of the material and is approximately taken as n times the value in air. Best-fitting curves of these data were derived according to Eq. (5), as shown in Fig. 2(a), and the values of the probe response parameters p and α_{eff} for the four samples are given in Table 1. The presence of alumina seems to have a significant influence on the PRF of the zirconia Raman band because of the difference in the optical properties between alumina and zirconia. The PRF obtained for the monoclinic band located at 190 cm^{-1} was almost coincident with that retrieved for the 180 cm^{-1} band. According to Eq. (11), the relevant optical parameters, the probe depths, can be obtained for these ZrO_2 polymorphs, as the results shown in Table 1. Although in this research the least square method was applied for fitting, a slight deviation, as well as scattering of the experimental data, was observed, which might be originated from the probe-sample interaction among the polycrystalline grain boundaries. In addition, it should be noted that the probe response function is dependent on the grain size of the material, and the probe depth decreases with decreasing grain size (e.g., in polycrystalline Al_2O_3)²⁹ because the presence of light multiple-reflections, refractions, and scattering at grain boundaries can

Table 1 Values of probe response parameters, p and α_{eff} , and respective probe depth obtained in four different zirconia-based samples.

	$p/\mu\text{m}$	$\alpha_{\text{eff}}/\mu\text{m}^{-1}$	$Z_d/\mu\text{m}$
$t\text{-ZrO}_2$	40	0.028	30.2
$m\text{-ZrO}_2$	10	0.026	17.3
$t\text{-ZTA}$	73	0.053	17.8
$m\text{-ZTA}$	60	0.050	18.5

strongly influence the material absorption through the dissipation of photon energy. These differences in probe geometry need to be taken into consideration for a recalibration for higher precision, when applying the PRFs for analysis in any material with a grain size significantly different from the current cases.

In order to study the in-plane probe size, both the untreated and the fully transformed TZP samples were respectively foiled with dotite to make a sharp interface, and then Raman spectral line scans were performed crossing the interface with and without using the confocal aperture (100 μm), as the schematic draft shown in the inset to Fig. 2(b). Figure 2(b) shows the corresponding variations of the normalized intensities of the 146 cm^{-1} Raman line and the 178 cm^{-1} band, respectively, in the line scans. Best-fitting curves of the obtained data collected on $t\text{-ZrO}_2$ and $m\text{-ZrO}_2$ demonstrated that the beam-waist radius on the focal plane was barely altered by the use of the confocal pinhole, showing only a slight reduction of the lateral probe size.

4.2 In-Depth Phase-Transformation Profile in Partially Transformed 3Y-TZP

4.2.1 Nondestructive assessment I: laser defocusing measurements

A series of PT 3Y-TZP that experienced different exposure times in autoclave was first nondestructively investigated according to the laser defocusing method. Raman spectra arising from $t\text{-}$ and $m\text{-ZrO}_2$ were collected by in-depth confocal scanning nearby the surface of each hip joint, by taking the spectrum from the sample surface (i.e., at $z = z_0 = 0$) as a reference. Consequently, the apparent variation of the monoclinic volume fraction, $V_{m,\text{obs}}(z_0)$, along the subsurface was determined from the Raman band intensities, according to Eq. (15). Figure 3 shows the variation of $V_{m,\text{obs}}(z_0)$ with the defocusing depth with respect to the sample surface, $z_0 = 0$, for three different TZP that underwent autoclaving at 121°C for 72, 84, and 132 h, respectively. Similar to the determination of PRF, a positive z_0 value refers to a translation of the focal plane below the free sample surface. As can be seen, with increasing autoclave time, the measured monoclinic volume fraction also increases.

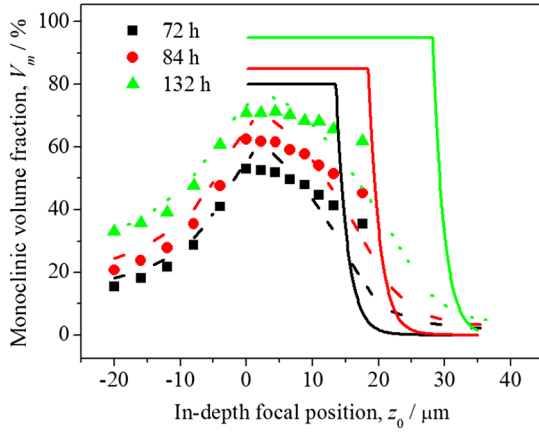


Fig. 3 (a) Plots of measured monoclinic volume fraction, $V_m(z_0)$, versus laser focal position, z_0 , as collected in three different partly transformed TZP. The best fit of the experimental data and the probe-deconvoluted V_m distribution [i.e., retrieved according to Eqs. (16) and (17)] are shown by the dash and the solid lines, respectively. The error involved in the Raman measurements is comparable with the size of the symbols used in the plots.

The apparent $V_{m,obs}(z_0)$ in general decreases with shifting the focal plane below the free surface, but the maximum

$$\bar{V}_m(z_0) = \begin{cases} \left[V_0 \int_0^{z_0} \Omega(z \leq z_0) G_m(z) dz + V_0 \int_{z_0}^{T_s} \Omega(z > z_0) G_m(z) dz \right. \\ \left. + \int_{T_s}^{\infty} V_0 \exp[-V(z - T_s)] \times \Omega(z > z_0) G_t(z) dz \right] / \left[\int_0^{z_0} \Omega(z \leq z_0) G_m(z) dz + \right. \\ \left. \int_{z_0}^{T_s} \Omega(z > z_0) G_m(z) dz + \int_{T_s}^{\infty} \Omega(z > z_0) G_t(z) dz \right] & (z_0 < T_s) \\ \left[V_0 \int_0^{T_s} \Omega(z \leq z_0) G_m(z) dz + \int_{T_s}^{z_0} V_0 \exp[-V(z - T_s)] \Omega(z \leq z_0) G_t(z) dz \right. \\ \left. + \int_{z_0}^{\infty} V_0 \exp[-V(z - T_s)] \times \Omega(z > z_0) G_t(z) dz \right] / \left[\int_0^{T_s} \Omega(z \leq z_0) G_m(z) dz + \right. \\ \left. \int_{T_s}^{z_0} \Omega(z \leq z_0) G_t(z) dz + \int_{z_0}^{\infty} \Omega(z > z_0) G_t(z) dz \right] & (z_0 \geq T_s) \end{cases}, \quad (17)$$

where the subscripts locate whether the parameter refers to the tetragonal or to the monoclinic phase (t and m , respectively). After introducing the probe parameters in Eq. (17), an iterative routine can be run to find the parameters V_0 , V , and T_s in order to match the experimentally determined $V_{m,obs}(z_0)$ functions retrieved from the defocusing measurements. The best-fitting results of this mathematical deconvolution procedure are also plotted in Fig. 3. Reliability of the obtained results will be discussed in the following sections by comparing different methods. It should be noted that in this defocusing measurement, the number of experimental data that can be collected depends on (or is limited by) both the minimum step of the translation of the stage in the depth direction ($0.5 \mu\text{m}$ in the current study) and the refractive index of the material. Therefore, application of this method to the analysis of very thin transformation layers will be ineffective, and the error involved with this kind of analysis certainly increases with decreasing sample thickness.

4.2.2 Nondestructive assessment II: controlled pinhole aperture method

Another nondestructive method is to control the confocal pinhole aperture to gradually alter the probe size with the laser

value may not be located exactly at the surface ($z_0 = 0$), which indicates a relatively high fraction of the monoclinic phase in the subsurface.

According to previously published results on the mechanism about the $t \rightarrow m$ transformation,^{10,30,31} in phase-transformation processes, the transformation is generally assumed to occur starting from the surface and propagating through the bulk with forming a layer of monoclinic phase of increasing thickness. As a result, polymorphic changes are maximized on the sample surface and vary rapidly with position along the z axis. Accordingly, the character of the profile function of $V_m(z)$ can be hypothesized as a monotonically structured one, as follows:

$$V_m(z) = \begin{cases} V_0 & (0 \leq z \leq T_s) \\ V_0 \exp[-V(z - T_s)] & (z > T_s) \end{cases}, \quad (16)$$

where V_0 represents the constant value of monoclinic fraction within a surface layer $0 \leq z \leq T_s$ (T_s : layer thickness) and V is a parameter dependent on the adopted autoclave conditions.

Equation (14) can then be rewritten for the in-depth scans by taking into account the PRFs for tetragonal and monoclinic bands as follows:

beam focus fixed on the sample surface. Raman spectra arising from t - and m - ZrO_2 were recorded as a function of the confocal aperture in a series of PT-TZP with various aging times. Figure 4(a) shows the corresponding variations of the intensity of the 178 cm^{-1} Raman band of m - ZrO_2 with increasing pinhole aperture, as measured in the TZP samples that underwent autoclave process for 60, 72, 84, 96, and 120 h, respectively. For comparison, results obtained on a fully transformed sample were also provided in this figure. As can be seen, responses to the change in the pinhole aperture (or probe size) for the series of PT-TZP samples are quite different, but can be rationalized. For the sample with the shortest exposure time, on increasing the pinhole aperture, the intensity increases promptly and then saturates to become independent of pinhole aperture, while intensity saturation appears to occur more slowly for longer exposure times. When the exposure time is >96 h, a difference could hardly be found among the results obtained in such samples (cf. 96 h, 120 h and fully transformed samples), which clearly indicates the limitation imposed by the probe size on the measurements. Figure 4(b) shows the variation of the obtained apparent monoclinic phase fractions as a function of the pinhole

aperture for the samples of 72- and 144-h aging. When the pinhole aperture increases, $V_{m,obs}$ gradually decreases, showing a slower rate of decrease for longer exposure time.

Theoretical curves can be derived from rewriting Eqs. (6) and (10), for the change in the pinhole aperture by taking into account the PRFs, as follows:

$$I_{obs}(\Phi) \propto \begin{cases} \int_0^t \int_0^{\rho_{max}} \frac{1}{B_m(z)} \exp\left[-2\frac{r^2}{B_m(z)}\right] r dr \times \Omega(\rho_{max} \leq \rho_0) G_m(z) dz \\ + \int_t^{T_s} \int_0^{\rho_0} \frac{1}{B_m(z)} \exp\left[-2\frac{r^2}{B_m(z)}\right] r dr \times \Omega(\rho_{max} \geq \rho_0) G_m(z) dz \\ + \int_{T_s}^{\infty} \int_0^{\rho_0} \frac{1}{B_t(z)} \exp\left[-2\frac{r^2}{B_t(z)}\right] r dr \times \exp[-V(z - T_s)] \times \Omega(\rho_{max} \geq \rho_0) G_t(z) dz & (t < T_s) \\ \int_0^{T_s} \int_0^{\rho_{max}} \frac{1}{B_m(z)} \exp\left[-2\frac{r^2}{B_m(z)}\right] r dr \times \Omega(\rho_{max} \leq \rho_0) G_m(z) dz \\ + \int_{T_s}^t \int_0^{\rho_{max}} \frac{1}{B_t(z)} \exp\left[-2\frac{r^2}{B_t(z)}\right] r dr \times \exp[-V(z - T_s)] \times \Omega(\rho_{max} \leq \rho_0) G_t(z) dz \\ + \int_t^{\infty} \int_0^{\rho_0} \frac{1}{B_t(z)} \exp\left[-2\frac{r^2}{B_t(z)}\right] r dr \times \exp[-V(z - T_s)] \times \Omega(\rho_{max} \geq \rho_0) G_t(z) dz & (t \geq T_s) \end{cases} \quad (18)$$

and

$$\overline{V}_m(\Phi) = \begin{cases} \left(V_0 \int_0^t \frac{B_m(z)}{4} \left\{ 1 - \exp\left[-2\frac{\rho_{max}^2}{B_m(z)^2}\right] \right\} \times \Omega(\rho_{max} \leq \rho_0) G_m(z) dz \right. \\ + V_0 \int_t^{T_s} \frac{B_m(z)}{4} \left\{ 1 - \exp\left[-2\frac{\rho_0^2}{B_m(z)^2}\right] \right\} \times \Omega(\rho_{max} > \rho_0) G_m(z) dz \\ \left. + \int_{T_s}^{\infty} \frac{B_t(z)}{4} \left\{ 1 - \exp\left[-2\frac{\rho_0^2}{B_t(z)^2}\right] \right\} \times V_0 \exp[-V(z - T_s)] \times \Omega(\rho_{max} > \rho_0) G_t(z) dz \right) / \\ \left(\int_0^t \frac{B_m(z)}{4} \left\{ 1 - \exp\left[-2\frac{\rho_{max}^2}{B_m(z)^2}\right] \right\} \times \Omega(\rho_{max} \leq \rho_0) G_m(z) dz \right. \\ + \int_t^{T_s} \frac{B_m(z)}{4} \left\{ 1 - \exp\left[-2\frac{\rho_0^2}{B_m(z)^2}\right] \right\} \times \Omega(\rho_{max} > \rho_0) G_m(z) dz \\ \left. + \int_{T_s}^{\infty} \frac{B_t(z)}{4} \left\{ 1 - \exp\left[-2\frac{\rho_0^2}{B_t(z)^2}\right] \right\} \times \Omega(\rho_{max} > \rho_0) G_t(z) dz \right) & (t < T_s) \\ \left(V_0 \int_0^{T_s} \frac{B_m(z)}{4} \left\{ 1 - \exp\left[-2\frac{\rho_{max}^2}{B_m(z)^2}\right] \right\} \times \Omega(\rho_{max} \leq \rho_0) G_m(z) dz \right. \\ + \int_{T_s}^t \frac{B_t(z)}{4} \left\{ 1 - \exp\left[-2\frac{\rho_{max}^2}{B_t(z)^2}\right] \right\} \times V_0 \exp[-V(z - T_s)] \times \Omega(\rho_{max} \leq \rho_0) G_t(z) dz \\ + \int_t^{\infty} \frac{B_t(z)}{4} \left\{ 1 - \exp\left[-2\frac{\rho_0^2}{B_t(z)^2}\right] \right\} \times V_0 \exp[-V(z - T_s)] \times \Omega(\rho_{max} > \rho_0) G_t(z) dz \right) / \\ \left(\int_0^{T_s} \frac{B_m(z)}{4} \left\{ 1 - \exp\left[-2\frac{\rho_{max}^2}{B_m(z)^2}\right] \right\} \times \Omega(\rho_{max} \leq \rho_0) G_m(z) dz \right. \\ + \int_{T_s}^t \frac{B_t(z)}{4} \left\{ 1 - \exp\left[-2\frac{\rho_{max}^2}{B_t(z)^2}\right] \right\} \times \Omega(\rho_{max} \leq \rho_0) G_t(z) dz \\ \left. + \int_{z_0}^{\infty} \frac{B_t(z)}{4} \left\{ 1 - \exp\left[-2\frac{\rho_0^2}{B_t(z)^2}\right] \right\} \times \Omega(\rho_{max} > \rho_0) G_t(z) dz \right) & (t \geq T_s) \end{cases}, \quad (19)$$

where the beam radii on $m - \text{ZrO}_2$ and $t - \text{ZrO}_2$, $B_m(z)$ and $B_t(z)$, have been calibrated as shown in Fig. 2(b).

Similarly, after introducing the probe parameters in Eq. (19), the parameters V_0 , V , and T_s can be determined from an iterative computational routine performed to match the experimentally determined $V_{m,obs}(\Phi)$ data, as the best-fitting results also shown in Fig. 4.

4.2.3 Destructive assessment: cross-sectional inspection

In order to examine the reliability of the above-obtained results, the investigated samples were sectioned by cutting perpendicular to the sample surface, and the cross-sections were well polished for Raman microscopy studies. A semiquantitative visualization of the near-surface phase-transformation phenomenon is given by the optical (laser) micrograph, as

shown in Fig. 5(a), according to a darker contrast in the near-surface (i.e., mainly monoclinic) zone with respect to the brighter tetragonal phase constituting the bulk area of the sample.

Raman spectral line scans were then carried out with crossing the dark layer along the in-depth z direction [cf. dot line in Fig. 5(a)], with the origin set at the free surface. Figure 5(b) shows the variation of the measured apparent $V_{m,obs}$ in the line scans for the TZP samples that experienced aging for 72, 96, and 144 h, respectively. In the cross-sectional scan, V_m keeps a high constant value nearby the free surface of the sample and then drops quickly below a given in-depth location. This result is consistent with the observation of the dark monoclinic layer, which also confirms the validity of the hypothesized trial function $V_m(z)$ in Eq. (16) for phase-transformation profiles. Occurrence of phase transformation starts from

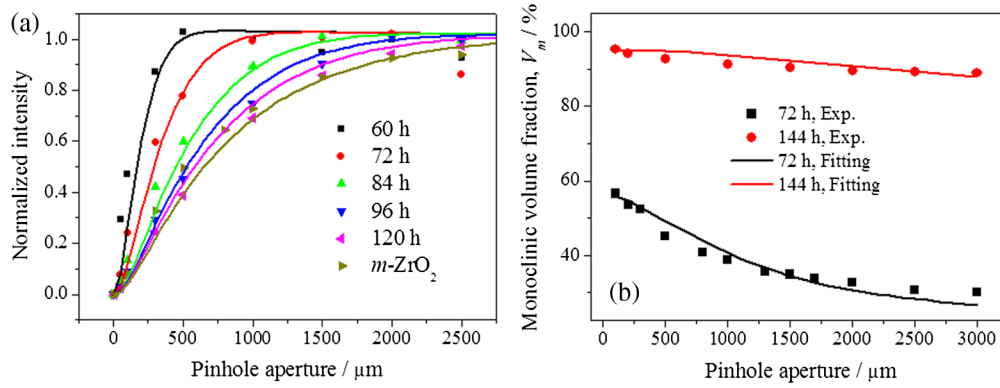


Fig. 4 Variation of (a) the relative intensity of the 178 cm^{-1} Raman band and (b) the monoic volume fraction with confocal aperture in a set of TZP samples with various exposure times in autoclave. Theoretical solid curves shown in (a) and (b) were calculated according to Eqs. (18) and (19), respectively.

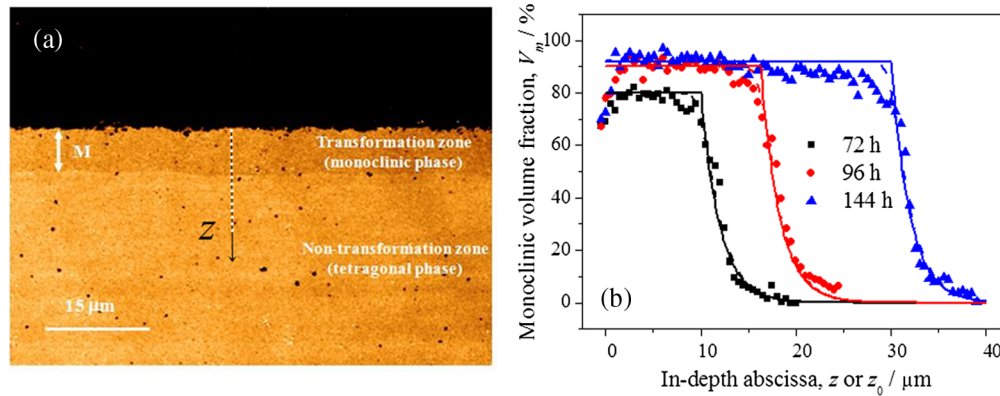


Fig. 5 (a) Typical laser micrograph showing the cross-section of an environmentally transformed zirconia. (b) Variation of $V_m(z_0)$ as a function of the distance from the free surface in the cross-sectional line scans performed on various 3Y-TZP samples with different exposure times in autoclave. The best fitting of the experimental data and the probe-deconvoluted V_m distributions [i.e., retrieved according to Eq. (20)] are shown by dash and solid lines, respectively.

the subsurface and advances inside the material by forming a layer-like monoclinic phase.

Note that by comparing the apparent $V_{m,obs}(z_0)$ distributions obtained by the in-depth defocusing measurements (data set shown in Fig. 3) and by scanning the cross-section of the same sample [data set shown in Fig. 5(b)], one can find that although both scanning procedures are affected by the finite size of the confocal probe, a clearly underestimated profile and less satisfactory curve-fitting can be noticed for the in-

depth scanning. This is because of a much larger in-depth size of the probe reaching depths far along the subsurface (i.e., with respect to the in-plane one), when the laser microprobe is focused on the joint surface.

Taking into account Eqs. (1) and (16), since the property distribution in the y direction is negligible for the current cases, Eq. (3) can be approximately rewritten for a cross-sectional line scan with the focal plane located on the cross-section as follows:

$$\bar{V}_m(z_0) = \frac{\int_{x=0}^{+\infty} \int_{z=0}^{T_s} V_0 \times \exp\left[-2\frac{(z-z_0)^2}{B_m^2}\right] G_m(x) dx dz + \int_{x=0}^{+\infty} \int_{z=T_s}^{+\infty} V_0 \times \exp[-V(z-T_s)] \times \exp\left[-2\frac{(z-z_0)^2}{B_t^2}\right] G_t(x) dx dz}{\int_{x=0}^{+\infty} \int_{z=0}^{T_s} G_m(x) \exp\left[-2\frac{(z-z_0)^2}{B_m^2}\right] dx dz + \int_{x=0}^{+\infty} \int_{z=T_s}^{+\infty} G_t(x) \exp\left[-2\frac{(z-z_0)^2}{B_t^2}\right] dx dz} \quad (20)$$

Accordingly, best-fitting to the experimental data shown in Fig. 5(b) can be performed and the parameters V_0 , V , and T_s can be determined. The results of the calculation are also shown in the same figure.

4.2.4 Dependence of the monoclinic layer thickness on exposure time in autoclave

Figure 6 shows a comparison between the T_s values (at increasing holding times in moist environment) as observed by the

cross-sectional inspection of the sample and those retrieved from a best-fitting routine applied to Eq. (17) by LDM and Eq. (19) by CPAM. The very close correspondence among the three phase-transformation profiles obtained by independent line scans along the z - and x axis and the consistency between the T_s values obtained by cross-sectional observation and those retrieved from the mathematical deconvolution procedure applied on the sample surface can be considered to be proofs for the consistency of the proposed spectroscopic procedure and for the validity of the PRF approach.

The depth of monoclinic phase, T_s , in response to the aging time, t_{aging} , can be empirically obtained from a nearly linear function.

$$T_s = 0.2986t_{\text{aging}} - 9.3333. \quad (21)$$

In the case of exposure time of 96 h, the monoclinic layer thickness ($T_s = 19 \mu\text{m}$) is comparable with the probe size ($Z_d = 17.3 \mu\text{m}$), so no more clear difference could be found when the exposure time further increased, which well explains the phenomena shown in Fig. 4(a). Because of this constraint of the finite probe size, when the monoclinic layer thickness is larger than the corresponding probe size, a gradual underestimation of the obtained T_s can be found (cf. Fig. 6) for CPAM.

Note that the relationship given by Eq. (21), which is valid for the present cases with the same autoclave conditions except for a change in the exposure time, may not be applicable if the autoclave condition is altered, e.g., temperature, degree of moisture, pressure, and so on. In addition, changes in grain size of the TZP sample can also result in an influence on the relation between T_s and t_{aging} . The thickness of the transformation layer is of importance because it might affect the residual stress fields developed on the bearing surface and thus the wear behavior of the material.³² For any specific TZP material, the response to aging may be distinct, but the phase-transformation profile can still be nondestructively analyzed by a combination of the two methods proposed here, which complement each other. The constraint of the finite probe size for CPAM in the case of thick materials can be circumvented by LDM, while the possible insufficient number of collectable data for the latter to analyze thin transformed layers in the sample could be avoided by systematically varying the pinhole aperture. In

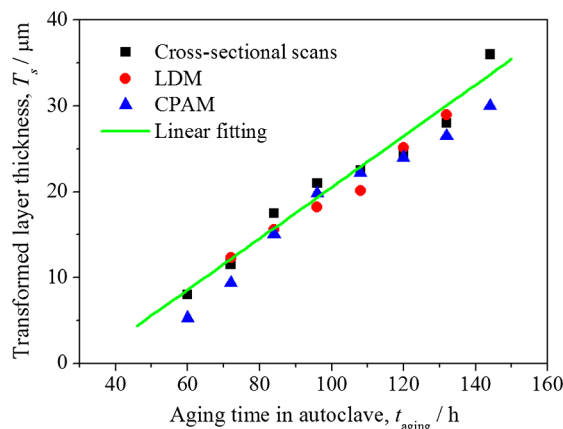


Fig. 6 Comparisons of the T_s values (at increasing holding times in moist environment) as obtained from three different methods applied to the same samples, retrieved from a best-fitting routine applied to Eq. (17).

addition, in practical analyses by Raman spectroscopy of retrieved hip joints, which generally cannot be sectioned, the above cross-sectional inspection is not feasible, and thus the phase-transformation analysis can only be obtained by the above two nondestructive methods.

Since we have now confirmed, according to the procedure shown in the previous sections, the validity of the proposed methods for evaluating the phase-transformation profiles in 3Y-TZP ceramics, it is possible to apply a similar iterative best-fitting procedure [i.e., according to Eqs. (17) and (19)] to the in-depth profile data set in order to retrieve the actual phase-transformation profile in more general and new hip-joint materials, the ZTA composites.

4.3 Nondestructive In-Depth Analysis of ZTA Composites

Two kinds of ZTA hip joint provided by different companies were investigated. The samples were put in autoclave at 121°C for 200 h, respectively. Figures 7(a) and 7(b) show the variations of the measured apparent monoclinic volume fraction with the focal position, as obtained by LDM when $\Phi = 100 \mu\text{m}$, and with increasing the pinhole aperture, as obtained by CPAM when $z_0 = 0$, respectively. A significant difference in the profile of monoclinic phase fraction can be seen from this figure between the two kinds of ZTA ceramics. The phenomena observed in sample ZTA-A are quite similar to the case of 3Y-TZP: $V_{m,\text{obs}}$ has a maximum at nearby the sample surface (or smallest pinhole aperture) and then gradually decreases with increasing the focal position or the pinhole aperture. However, in sample ZTA-D, with increasing focal depth, the apparent $V_{m,\text{obs}}$ first increases till about $z_0 = 15 \mu\text{m}$ and then gradually decreases, while $V_{m,\text{obs}}$ continuously rises in response to increasing the pinhole aperture. For comparison, untreated ZTA-A and ZTA-D samples were also analyzed. No pronounced change in the obtained value of $V_{m,\text{obs}}$ was found for sample ZTA-A, while a steep decrease in the measured $V_{m,\text{obs}}$ was found along the in-depth direction (cf. Fig. 7), indicating a prior occurrence of phase transformation nearby the surface before autoclave.

For sample ZTA-A, since phase transformation should start from the sample surface, Eq. (16) can still be treated as a trial function for the character of the transformation profile. Nevertheless, for sample ZTA-D, because of the pre-existence of phase transformation on the surface, polymorphic changes are maximized below the surface [cf. Fig. 7(b) V_m minimizes when $\Phi = 400 \mu\text{m}$ for untreated ZTA-D], and thus the transformation profile is altered. Based on the experimental data and the transformation mechanism, the character of the profile function of $V_m(z)$ can be hypothesized as follows:

$$V_m(z) = \{V_0 \exp[-V(z - T_s)] + V_1\} \times \text{ArcTan}[V_2 z], \quad (22)$$

where V_1 and V_2 are treated as variables. Note that although Eq. (22) might not represent exactly the function that gives the real transformation profile, the values of the two functions at different z can give a good approximation, provided that a satisfactory agreement between calculation and experiments is found taking advantage of a sufficient number of available experimental data.

Accordingly, Eqs. (17) and (19) can be modified by taking into account the transformation profile shown in Eq. (22). After

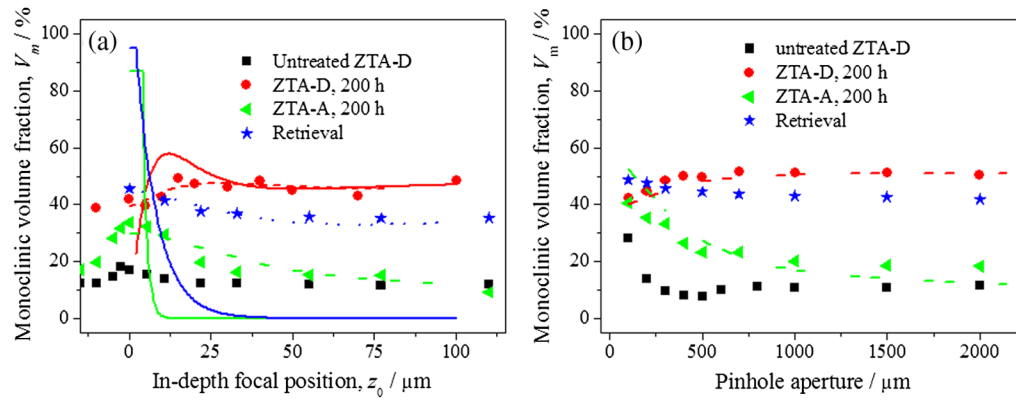


Fig. 7 Variation of measured monoclinic volume fraction, $V_m(z_0)$, with (a) laser focal position, z_0 , and (b) confocal aperture as collected in different ZTA samples. The best fit of the experimental data and the probe-deconvoluted V_m distribution are shown by the dash and the solid lines, respectively.

introducing the probe parameters for ZTA, similarly, an iterative routine can be run to find the parameters in order to match the experimentally determined $V_{m,obs}(z_0)$ functions (i.e., retrieved from measurements on ZTA-A and ZTA-D by LDM and CPAM). Results of such best-fitting procedure and the deconvoluted curves are also shown in Figs. 7(a) and 7(b), respectively. With respect to monolithic zirconia materials, hydrothermal degradation of the zirconia phase in the composites after exposure to humid atmosphere is significantly slower.

As has previously been pointed out,³² during the sintering process, hydroxylated areas may survive in the sintered body into agglomerations of raw powder mixture and become potential nuclei from which polymorphic transformation originates and spreads on the sample surface. Hydrothermal attack to the tetragonal ZrO_2 phase on the composite progresses slowly at the expenses of a fast formation rate of oxygen vacancies in the alumina matrix lattice.³³ Moreover, local stoichiometry gradients play a major role in the evolution with time of surface nuclei as preferential sites of polymorphic transformation. Therefore, the difference in the transformation profile, or in phase stability characteristics, originates from the different content of stabilizing agents added to the raw powder mixtures of the two materials (i.e., a small fraction and null in ZTA-D and ZTA-A, respectively). In other words, the microstructural design of ZTA-D enables control of the initial amount of monoclinic phase in the material and ensures surface stability when embedded in a hydrothermal environment. As the purpose of this paper is to examine the validity of two nondestructive approaches for a reliable analysis of the transformation profile, further studies on the influence of autoclave temperature and other factors on the transformation mechanisms can be made by a systematic investigation by these methods, but will not be discussed here.

For completeness, an investigation on the main-wear-zone of an *in vivo* ZTA ball retrieved as a load-bearing component against a polyethylene cup was also performed by LDM and CPAM, as the obtained data plots of $V_{m,obs}$ versus z_0 or Φ , and related deconvolution of the transformation profile also shown in Fig. 7. As can be seen, the retrieved ZTA ball shows a very similar change in V_m as sample ZTA-A, except for a higher value of monoclinic volume fraction because of a longer exposure time in biological environment.

Finally, it is worth mentioning that this paper was devoted to the analyses of highly graded phase-transformation profiles along the hip-joint subsurface, but the methods can also be

applied to quantitatively analyze other physical, chemical, or mechanical information contained in a Raman spectrum, e.g., oxygen off-stoichiometry or residual stresses stored in the constituent components of zirconia-based ceramics.

5 Conclusion

In this paper, we compared two different nondestructive approaches with the aid of a mathematical probe deconvolution procedure for obtaining highly graded phase-transformation profiles along the hip-joint subsurface by confocal Raman microprobe technique in various PT TZP and ZTA ceramics subjected to different exposure times in autoclave. The respective probe response functions for selected Raman bands of both tetragonal and monoclinic ZrO_2 polymorphs in TZP and ZTA were determined according to the variation of Raman spectral intensity as a function of focal depth. Based on the sets of apparent $V_{m,obs}$ collected on the same material as a function of pinhole aperture and focal depth, respectively, the real transformation profiles were retrieved through a best-fitting iterative routine of Raman experimental data, and the reliability of the obtained results was confirmed by a destructive cross-sectional inspection by both laser optical microscope and Raman spectral line scans. Finally, studies of two kinds of commercially available ZTA hip joints and a retrieved one show a strong dependence of the transformation profiles on the presence of stabilizing agents, demonstrating the applicability of the methods to different zirconia-based ceramics and, concurrently, also the possibility of avoiding cutting of retrieved medical samples.

References

1. I. C. Clarke et al., "Current status of zirconia used in total hip implants—clinical and laboratory studies," *J. Bone Joint Surg. Am.* **85-A**(Suppl 4), 73–84 (2003).
2. R. J. Kohal, M. Wolkewitz, and C. Mueller, "Alumina-reinforced zirconia implants: survival rate and fracture strength in a masticatory simulation trial," *Clin. Oral Implants Res.* **21**(12), 1345–1352 (2010).
3. M. Kuntz, "Validation of a new high performance alumina matrix composite for use in total joint replacement," *Semin. Arthroplasty* **17**(3–4), 141–145 (2006).
4. K. Tanaka et al., "Phase stability after aging and its influence on pin-on-disk wear properties of Ce-TZP/ Al_2O_3 nanocomposite and conventional Y-TZP," *J. Biomed. Mater. Res.* **67A**(1), 200–207 (2003).
5. B. Cales, Y. Stefani, and E. Lilley, "Long-term *in vivo* and *in vitro* aging of a zirconia ceramic used in orthopaedy," *J. Biomed. Mater. Res.* **28**(5), 619–624 (1994).

6. K. Haraguchi et al., "Phase transformation of a zirconia ceramic head after total hip arthroplasty," *J. Bone Joint Surg. Br.* **83**(7), 996–1000 (2001).
7. J. Masonis et al., "Zirconia femoral head fractures: a clinical and retrieval analysis," *J. Arthroplasty* **19**(7), 898–905 (2004).
8. R. Petry, M. Schmitt, and J. Popp, "Raman spectroscopy—a prospective tool in the life sciences," *Chem. Phys. Chem.* **4**(1), 14–30 (2003).
9. G. Pezzotti and A. A. Porporati, "Raman spectroscopic analysis of phase-transformation and stress patterns in zirconia hip joints," *J. Biomed. Opt.* **9**(2), 372–384 (2004).
10. V. Sergo, "Room-temperature aging of laminate composites of alumina/3-mol%-Yttria-stabilized tetragonal zirconia polycrystals," *J. Am. Ceram. Soc.* **87**(2), 247–253 (2004).
11. G. Pezzotti, "Raman piezo-spectroscopic analysis of natural and synthetic biomaterials," *Anal. Bioanal. Chem.* **381**(3), 577–590 (2005).
12. G. Pezzotti et al., "Fluorescence spectroscopic analysis of surface and sub-surface residual stress fields in alumina hip joints," *J. Biomed. Opt.* **11**(4), 24009–24018 (2006).
13. C. Moura et al., "Raman spectra and structural analysis in ZrOxNy thin films," *Thin Solid Films* **515**(3), 1132–1137 (2006).
14. G. Pezzotti, K. Yamada, and S. Sakakura, "Raman spectroscopic analysis of advanced ceramic composite for hip prosthesis," *J. Am. Ceram. Soc.* **91**(4), 1199–1206 (2008).
15. G. Pezzotti et al., "Fracture toughness analysis of advanced ceramic composite for hip prosthesis," *J. Am. Ceram. Soc.* **92**(8), 1817–1822 (2009).
16. J. M. Tabares and M. J. Anglada, "Quantitative analysis of monoclinic phase in 3Y-TZP by Raman spectroscopy," *J. Am. Ceram. Soc.* **93**(6), 1790–1795 (2010).
17. K. Fukatsu et al., "Kinetics and the role of off-stoichiometry in the environmentally driven phase transformation of commercially available zirconia femoral heads," *Acta Biomater.* **8**(4), 1639–1647 (2012).
18. N. Djaker et al., "Zirconia dental implants degradation by confocal Raman microspectroscopy: analytical simulation and experiments," *Biomed. Opt. Express* **4**(5), 725–731 (2013).
19. F. E. Pfefferkorn et al., "Laser-assisted machining of magnesia-partially-stabilized zirconia," *J. Manuf. Sci. Eng.* **126**(1), 42–51 (2004).
20. M. Born and E. Wolf, *Principles of Optics*, 6th ed., Pergamon Press, Oxford (1985).
21. A. Atkinson and S. C. Jain, "Spatially resolved stress analysis using Raman spectroscopy," *J. Raman Spectrosc.* **30**(10), 885–891 (1999).
22. W. Zhu and G. Pezzotti, "Spatially resolved stress analysis in Al₂O₃/3Y-TZP multilayered composites using confocal fluorescence spectroscopy," *Appl. Spectrosc.* **59**(8), 1042–1048 (2005).
23. S. Nakashima and H. Harima, "Raman investigation of SiC polytypes," *Phys. Stat. Sol. A* **162**(1), 39–64 (1997).
24. K. J. Baldwin and D. N. Batchelder, "Confocal Raman microspectroscopy through a planar interface," *Appl. Spectrosc.* **55**(5), 517–524 (2001).
25. J. L. Bruneel, J. C. Lassegue, and C. Sourisseau, "In-depth analyses by confocal Raman microspectrometry: experimental features and modeling of the refraction effects," *J. Raman Spectrosc.* **33**(10), 815–828 (2002).
26. X. Y. Zhao and D. Vanderbilt, "Phonons and lattice dielectric properties of zirconia," *Phys. Rev. B* **65**(7), 075105 (2002).
27. G. H. Watson, W. B. Daniels, and C. S. Wang, "Measurements of Raman intensities and pressure dependence of phonon frequencies in sapphire," *J. Appl. Phys.* **52**(2), 956–958 (1981).
28. G. Katagiri et al., "Direct determination by a Raman microprobe of the transformation zone size in Y₂O₃-containing tetragonal ZrO₂ polycrystals," *Adv. Ceram.* **24**, 537–544 (1988).
29. K. Wan et al., "Quantitative evaluation of probe response functions for Raman and fluorescence bands of single-crystalline and polycrystalline Al₂O₃," *J. Phys. D: Appl. Phys.* **43**(20), 205501 (2010).
30. M. Yoshimura et al., "Role of H₂O on the degradation process of Y-TZP," *J. Mater. Sci.* **6**(4), 465–67 (1987).
31. R. H. Hannink, P. M. Kelly, and B. C. Muddle, "Transformation toughening in zirconia-containing ceramics," *J. Am. Ceram. Soc.* **83**(3), 461–487 (2000).
32. G. Pezzotti, *Advanced Materials for Joint Implants*, 1st ed., Pan Stanford, Singapore (2013).
33. G. Pezzotti et al., "On the role of oxygen vacancies and lattice strain in the tetragonal to monoclinic transformation in alumina/zirconia composites and improved environmental stability," *Biomaterials* **31**(27), 6901–6908 (2010).